

1 Supplement for manuscript

2 **Measurement report: *Characterization of severe spring haze***  
3 ***episodes and influences of long-range transport in the Seoul***  
4 ***metropolitan area in March 2019***

5

6 Hwajin Kim<sup>1,2</sup>, Qi Zhang<sup>3</sup>, Yele Sun<sup>4</sup>

7 <sup>1</sup>Center for Environment, Health and Welfare Research, Korea Institute of Science and Technology, Seoul, 02792,  
8 Korea

9 <sup>2</sup>Department of Energy and Environmental Engineering, University of Science and Technology, Daejeon, 34113,  
10 Korea

11 <sup>3</sup>Department of Environmental Toxicology, University of California, Davis, CA 95616, USA

12 <sup>4</sup>State Key Laboratory of Atmospheric Boundary Layer Physics and Atmospheric Chemistry, Institute of  
13 Atmospheric Physics, Chinese Academy of Sciences, Beijing 100029, China

14 \*Correspondence to: Hwajin Kim (hjkim@kist.re.kr)

15

16

17

18

19

20

21

22

23

24

25

26

27

28

29

30 **Table S1.** Average ( $\pm 1$  standard deviation), minimum and maximum concentrations of the  
31 particulate matter (PM<sub>1</sub>) species and the total PM<sub>1</sub> mass over the whole campaign, and the  
32 average contribution of each of the PM<sub>1</sub> species to the total PM<sub>1</sub> mass.

	Average conc. $\pm$ one standard deviation ( $\mu\text{g m}^{-3}$ )	Minimum conc. ( $\mu\text{g m}^{-3}$ )	Maximum conc. ( $\mu\text{g m}^{-3}$ )	Fraction of total PM <sub>1</sub> (%)	Detection limit (3min/ 6min) ( $\mu\text{g m}^{-3}$ )
Organics	13.3 $\pm$ 7.51	1.29	45.0	38	0.03/0.02
Nitrate	10.6 $\pm$ 9.68	0.21	52.0	30	0.01/0.01
Sulfate	4.20 $\pm$ 3.49	0.60	20.0	12	0.01/0.01
Ammonium	4.70 $\pm$ 3.99	0.28	21.2	13	0.02/0.01
Chloride	0.60 $\pm$ 0.54	0	4.03	2	0.00/0.00
Black carbon	1.60 $\pm$ 0.93	0.05	5.55	5	0.1/0.05
Total PM <sub>1</sub>	35.1 $\pm$ 23.8	3.85	129	-	0.05/0.03

33

34

35

36

37

38

39

40

41

42

43

44

45

46

47 **Table S2.** Comparison of the average O/C, H/C, and OM/OC ratios of total OA and the four OA  
 48 factors identified from PMF analysis calculated using the Aiken-Ambient method (Aiken et al.,  
 49 2008) and the improved Canagaratna-Ambient method (Canagaratna et al., 2015).

50

Species	Ratio	Aiken-Ambient	Canagaratna-Ambient
OA	O/C	0.41	0.52
	H/C	1.45	1.61
	OM/OC	1.70	1.86
HOA	O/C	0.08	0.10
	H/C	1.97	1.88
	OM/OC	1.29	1.33
COA	O/C	0.10	0.12
	H/C	1.74	1.88
	OM/OC	1.29	1.33
SFOA	O/C	0.41	0.53
	H/C	1.41	1.55
	OM/OC	1.71	1.87
LO-OOA1	O/C	0.47	0.59
	H/C	1.45	1.61
	OM/OC	1.76	1.93
LO-OOA2	O/C	0.50	0.65
	H/C	1.45	1.62
	OM/OC	1.81	2.02
MO-OOA1	O/C	0.99	0.99
	H/C	1.56	1.56
	OM/OC	2.46	2.46
MO-OOA2	O/C	0.93	1.11
	H/C	1.20	1.32
	OM/OC	2.44	2.69

51

52

53

54

55

56

57 **Table S3.** Expected(deLaeter et al., 2003) and calculated lead isotopic ratios from linear fits  
58 (Figs. Sx and x); slope (m) and Pearsons R are shown.

	Natural Isotope Ratio	Open signal				Closed signal			
		V-mode		W-mode		V-mode		W-mode	
		m	R	m	R	m	R	m	R
$^{206}\text{Pb}^+/^{208}\text{Pb}^+$	0.46	0.48	0.92	0.41	0.63	0.44	0.84	0.32	0.36
$^{207}\text{Pb}^+/^{208}\text{Pb}^+$	0.422	0.45	0.77	0.37	0.5	0.36	0.42	0.22	0.18
$^{206}\text{Pb}^{++}/^{208}\text{Pb}^{++}$	0.46	0.29	0.06	0.35	0.08	.	.	0.04	0
$^{207}\text{Pb}^{++}/^{208}\text{Pb}^{++}$	0.422	0.4	0.33	0.01	0.03	0.05	0.39	0.01	0.02

59

60

61

62

63

64

65

66

67

68

69

70

71

72

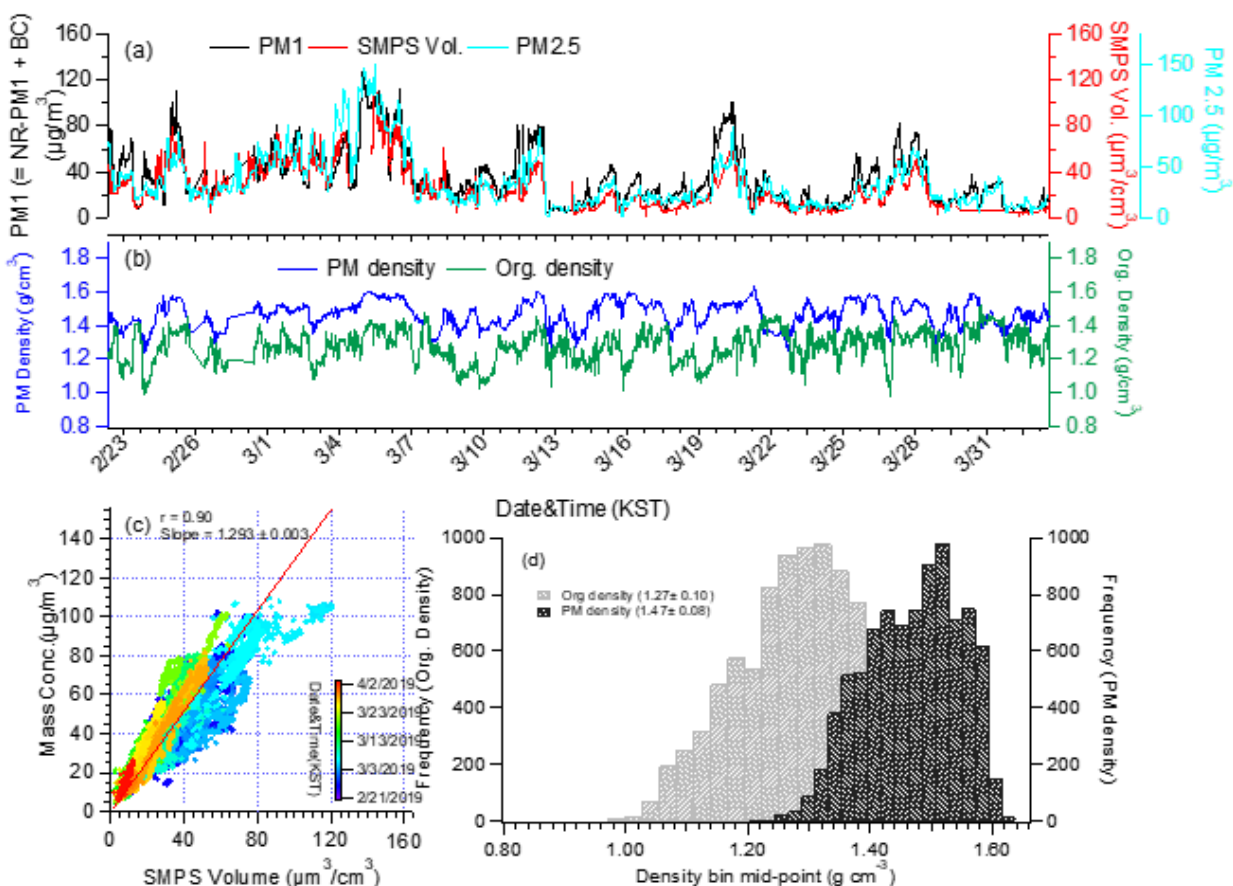
73

74

75

76

77  
78



79  
80

81 **Figure S1.** (a) Time series of total particulate matter ( $\text{PM}_{10}$ ), scanning mobility particle sizer  
82 (SMPS) volume concentrations and  $\text{PM}_{2.5}$  mass concentration measured at Gireum site ; (b)  
83 Time series of the organic aerosol density estimated using the method reported in Kuwata et al.  
84 (2012)

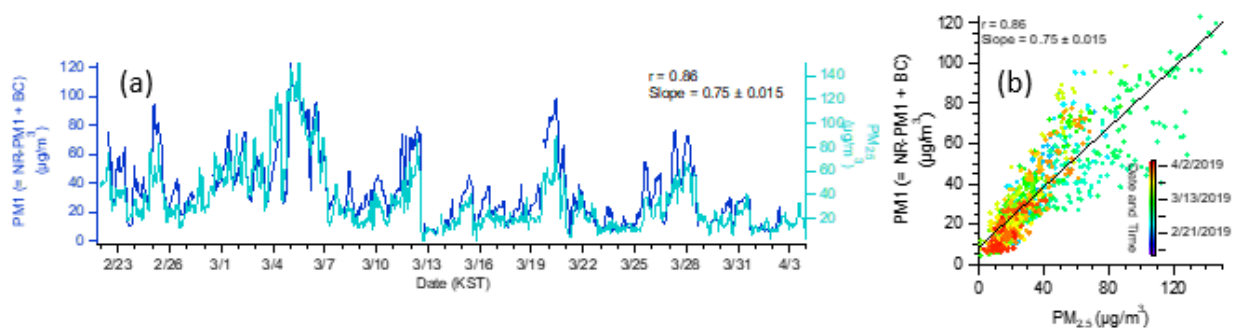
85 
$$\rho_{\text{org}} = [12 + 1 \cdot (\text{H}/\text{C}) + 16 \cdot (\text{O}/\text{C})] / [7 + 5 \cdot (\text{H}/\text{C}) + 4.15 \cdot (\text{O}/\text{C})]$$

86 and bulk aerosol density estimated from the measured chemical composition, known inorganic  
87 species density and the organic density estimated above (Zhang et al., 2005). (c) Scatter plot of  
88 the total  $\text{PM}_{10}$  mass (NR- $\text{PM}_{10}$  plus BC) versus SMPS volume, where the NR- $\text{PM}_{10}$  mass  
89 concentrations have been determined using the composition-dependent collection efficiencies; (d)

90 histogram of organic aerosol density (average =  $1.27 \text{ g cm}^{-3}$ ) and bulk aerosol density (average =  
91  $1.47 \text{ g cm}^{-3}$ ).

92

93



94

95

96

97

98

99

100 **Figure S2.** (a) Time series of total particulate matter (PM1) concentration and PM2.5 mass  
101 concentration measured at Gireum site (b) Scatter plot of total PM1 mass (NR-PM1 plus BC)  
102 versus PM2.5 mass.

103

104

105

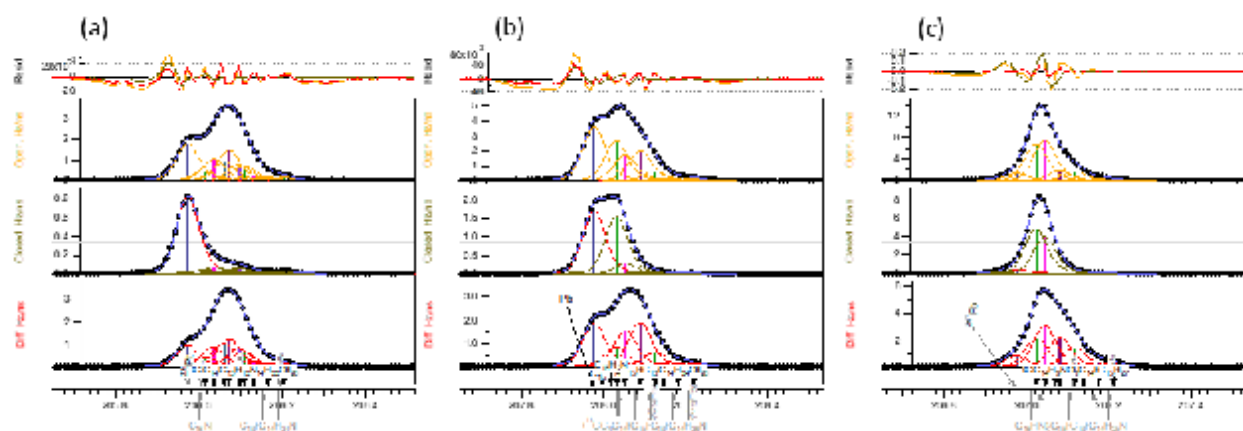
106

107

108

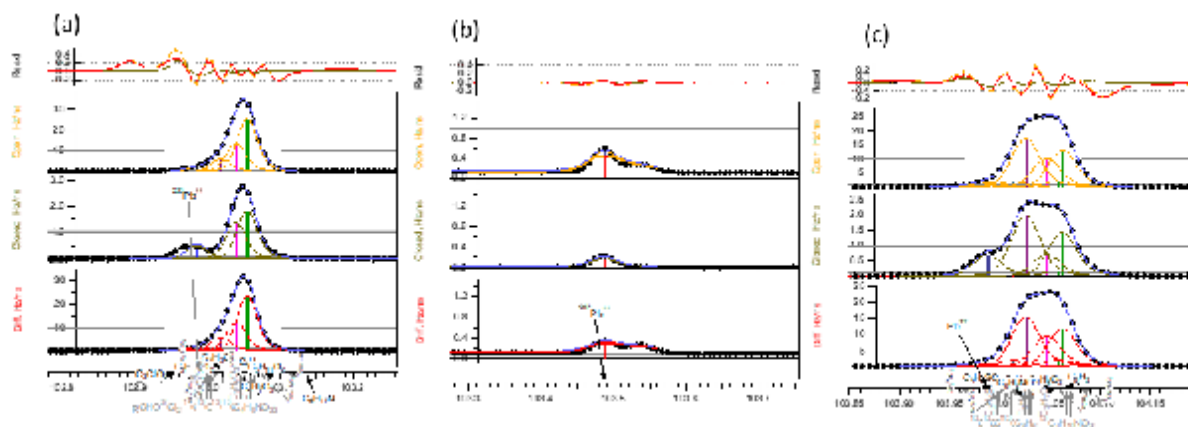
109

110  
111  
112  
113  
114  
115  
116



117  
118

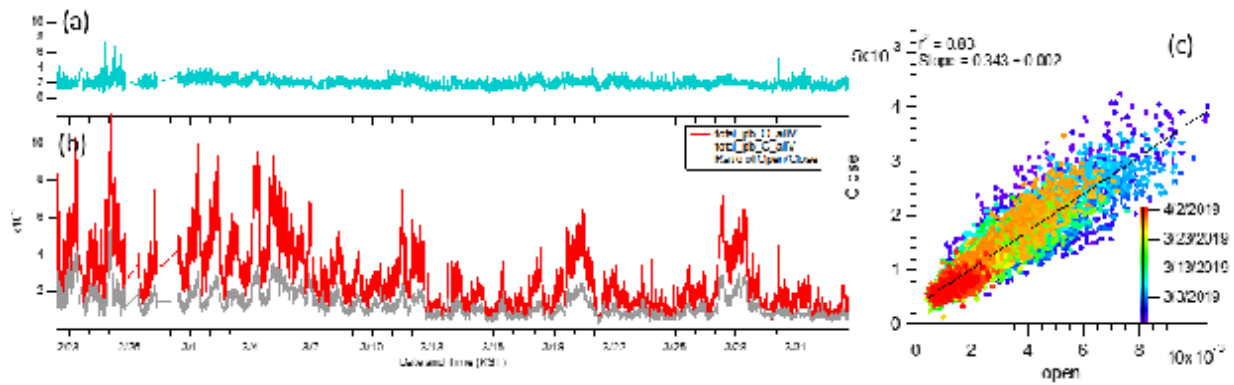
119 **Figure S3.** 2.5 minute averaged open V mode mass spectra at  $m/z$  206, 207, 208 during Haze  
120 period at KIST site. Black lines and circles correspond to the HRAMS raw signal. Yellow  
121 (open), black(closed) and red(diff) are modified Gaussian functions that represent the signal of  
122 individuals ions whose exact mass is indicated by the vertical black lines. The height of the  
123 vertical lines corresponds to the peak height of the modified Gaussian functions. Purple lines  
124 are the sum of the individual ion peaks and represent the fitted total signal at the given nominal  
125  $m/z$ .



126  
 127 Figure S3. 2.5 minute averaged open V mode mass spectra at m/z 103, 103.5 and 104 during  
 128 Haze period at KIST site. Black lines and circles correspond to the HRAMS raw signal.  
 129 Yellow (open), black(closed) and red(diff) are modified Gaussian functions that represent the  
 130 signal of individuals ions whose exact mass is indicated by the vertical black lines. The height  
 131 of the vertical lines corresponds to the peak height of the modified Gaussian functions. Purple  
 132 lines are the sum of the individual ion peaks and represent the fitted total signal at the given  
 133 nominal m/z.

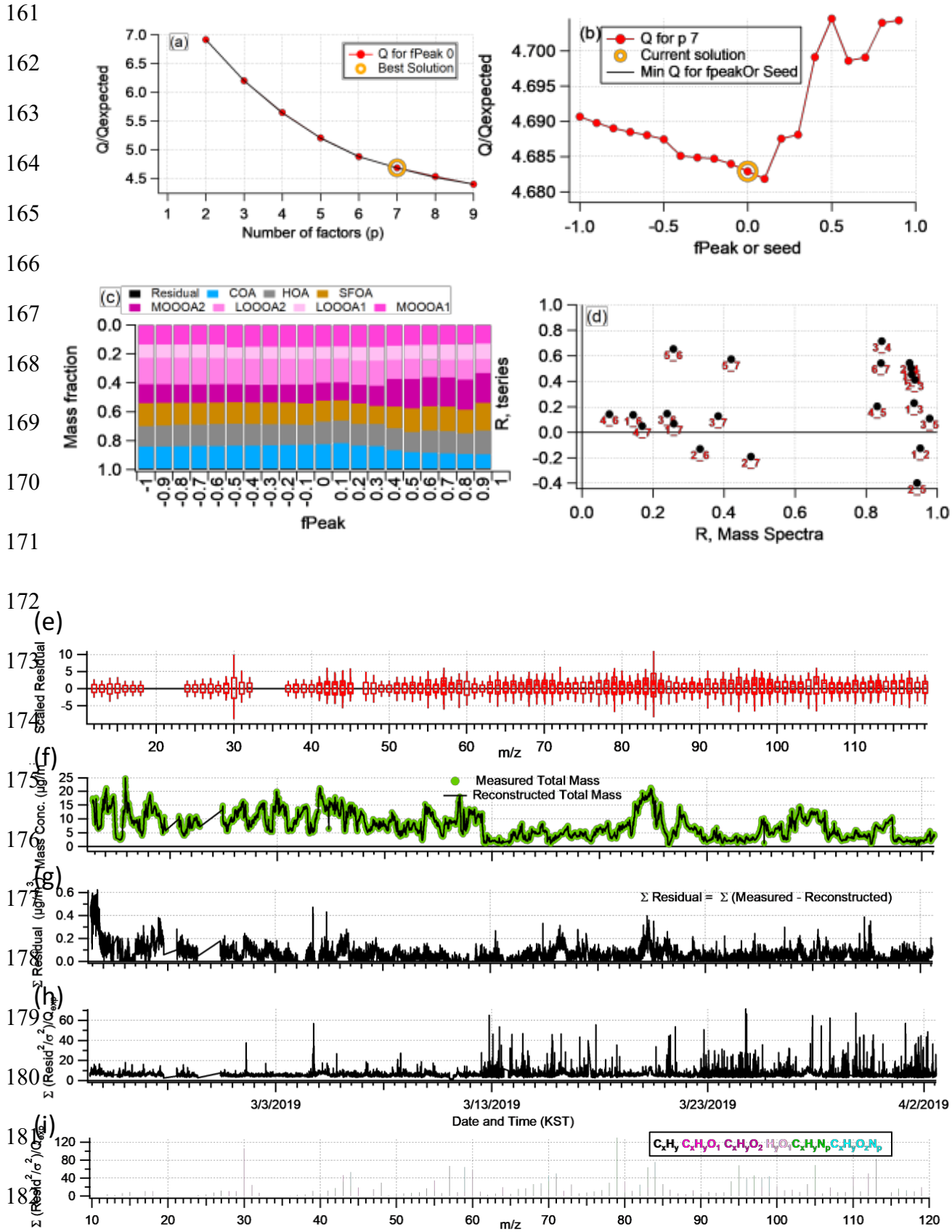
134  
 135  
 136  
 137  
 138  
 139  
 140





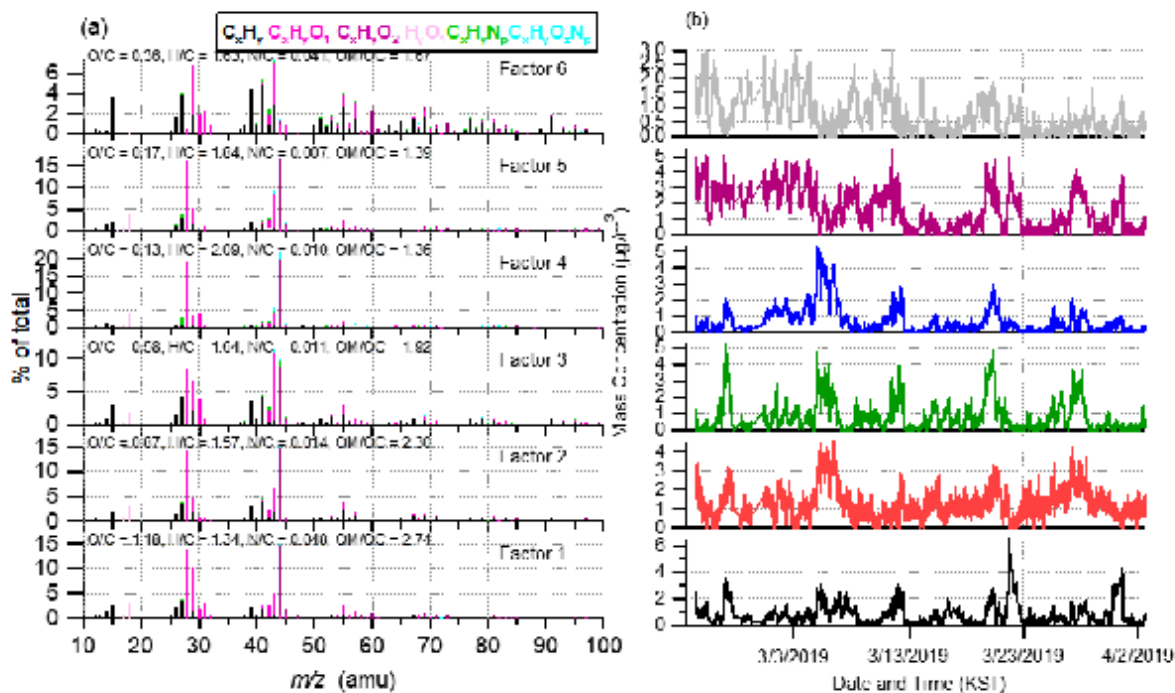
141  
 142  
 143  
 144  
 145  
 146  
 147  
 148  
 149  
 150  
 151  
 152  
 153  
 154  
 155  
 156  
 157  
 158  
 159  
 160

**Figure S5. (a,b)** Time series of total open (red), closed (black) signal of lead from Vmode and the ratio between open and close (terquid) total signal of lead from V mode; and (c) Scatter plot of total open and close signal of lead from Vmode data. Note that total open and close signals were calculated as the sum of the  $^{208}\text{Pb}^+$ ,  $^{207}\text{Pb}^+$ ,  $^{206}\text{Pb}^+$ ,  $^{208}\text{Pb}^{++}$ ,  $^{207}\text{Pb}^{++}$  and  $^{206}\text{Pb}^{++}$ .

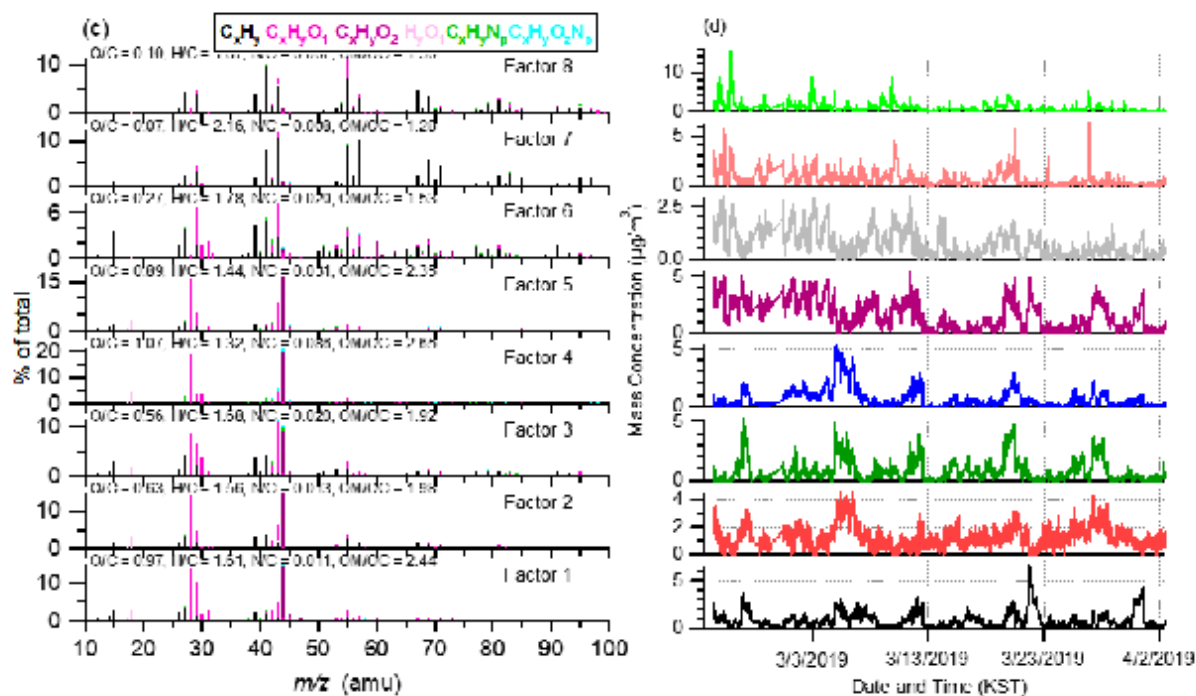


183

184 **Figure S6.** Summary of the key diagnostic plots of the chosen 7-factor from PMF analysis of the  
185 organic aerosol fraction: **(a)**  $Q/Q_{exp}$  as a function of the number of factors ( $p$ ) explored in PMF  
186 analysis, with the best solution denoted by the open orange circle. Plots **b-i** are for the chosen  
187 solution set, containing 7 factors: **(b)**  $Q/Q_{exp}$  as a function of fPeak; **(c)** mass fractional  
188 contribution to the total mass of each of the PMF factors, including the residual (in purple), as a  
189 function of fPeak; **(d)** Pearson's  $r$  correlation coefficient values for correlations among the time  
190 series and mass spectra of the PMF factors. Here, 1 = MO-OOA1, 2 = LO-OOA1, 3 = LO-OOA2,  
191 4 = MO-OOA2, 5 = SFOA, 6 = HOA, 7 = COA; **(e)** box and whiskers plot showing the  
192 distributions of scaled residuals for each  $m/z$ ; **(f)** time series of the measured mass and the  
193 reconstructed mass from the sum of the 6 factors; **(g)** time series of the variations in the residual  
194 (= measured – reconstructed) of the fit; **(h)** the  $Q/Q_{exp}$  for each point in time; **(i)** the  $Q/Q_{exp}$   
195 values for each fragment ion.



196



197

198

199

200 **Figure S7.** Overview of two other solution (6 factor and 8 factor solution) sets from PMF  
201 analysis: **(a)(b)** High resolution mass spectra and time series of the different OA factors from the  
202 6-factor solution; **(c)(d)** High resolution mass spectra and time series of the different OA factors  
203 from the 8-factor solution

204

205

206

207

208

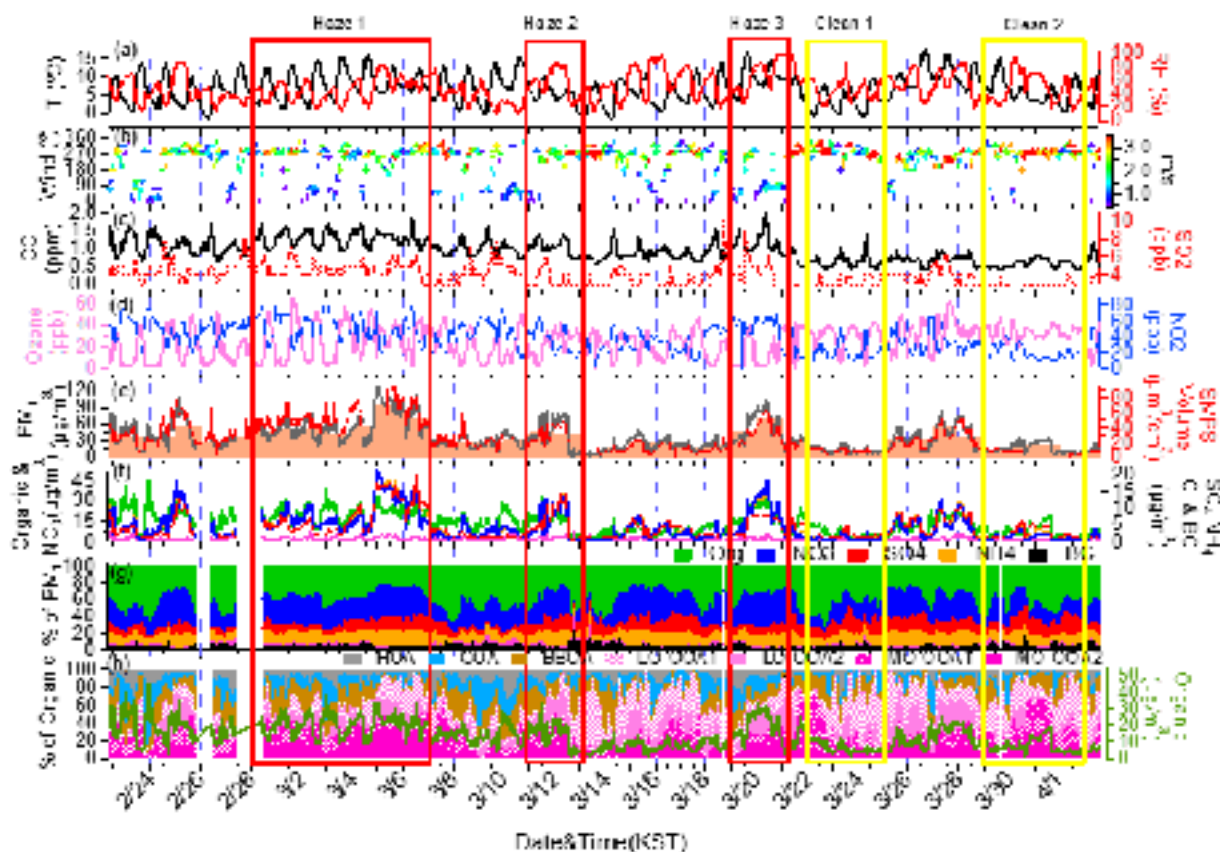
209

210

211

212

213



214

215

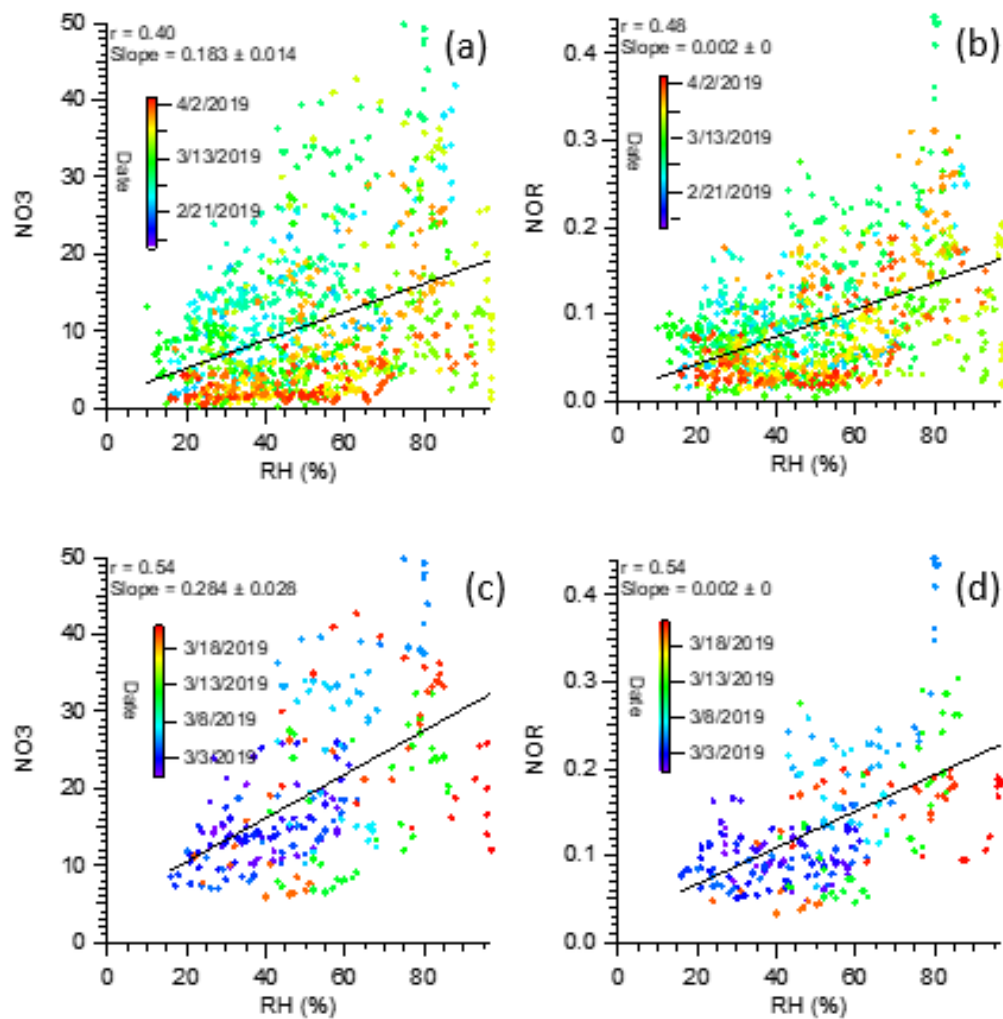
216 **Figure S8.** Overview of the temporal variations of submicron aerosols at the Korea Institute of  
 217 Science and Technology (KIST) in SMA from Feb. 22 to April 2 including three haze (red box)  
 218 and two clean (yellow box) period: **(a)** Time series of ambient air temperature (T) and relative  
 219 humidity (RH); **(b)** Time series of wind direction (WD), with colors showing different wind  
 220 speeds (WS); **(c)** Time series of CO and SO<sub>2</sub>; **(d)** Time series of O<sub>3</sub>, and NO<sub>2</sub>; **(e)** Time series of  
 221 total particulate matter (PM<sub>1</sub>), scanning mobility particle sizer (SMPS) volume concentrations  
 222 and also shown are the 24 h averaged PM<sub>1</sub>+BC with bars. **(f)** Time series of the organic (Org.),  
 223 nitrate (NO<sub>3</sub><sup>-</sup>), sulfate (SO<sub>4</sub><sup>2-</sup>), ammonium (NH<sub>4</sub><sup>+</sup>) and BC aerosols; **(g)** Time series of the mass  
 224 fractional contribution of organic aerosols (Org.), nitrate (NO<sub>3</sub><sup>-</sup>), sulfate (SO<sub>4</sub><sup>2-</sup>), ammonium  
 225 (NH<sub>4</sub><sup>+</sup>), chloride (Cl<sup>-</sup>), and BC to total PM<sub>1</sub> together with isoprene and toluene time series; **(h)**  
 226 Time series of each factor derived from the positive matrix factorization (PMF) analysis

227

228

229

230



231

232

233

234

235 **Figure S9.** Scatterplot of the variations of NOR and NO3 as a function of RH (a)(b) during  
236 entire period; (c) (d) during haze period.

237

238

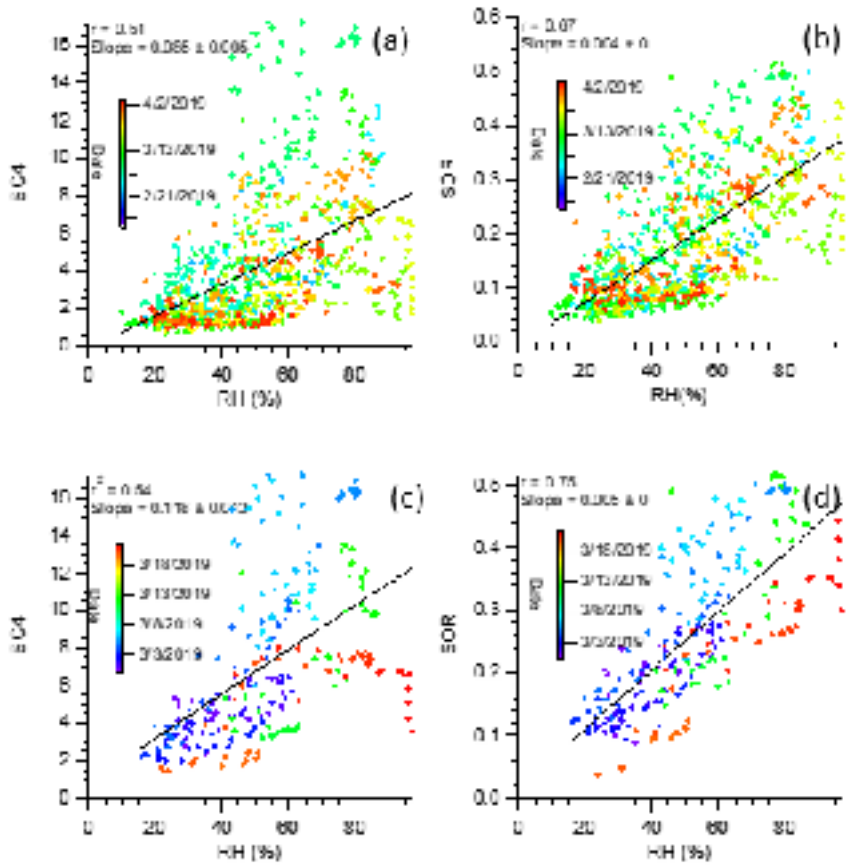
239

240

241

242

243



244

245

246

247

248



249 **Figure S10.** Scatterplot of the variations of SOR and SO<sub>4</sub> as a function of RH **(a)(b)** during  
 250 entire period; **(c) (d)** during haze period.

251  
 252  
 253  
 254  
 255  
 256  
 257  
 258  
 259  
 260  
 261  
 262  
 263  
 264  
 265  
 266  
 267  
 268  
 269  
 270  
 271

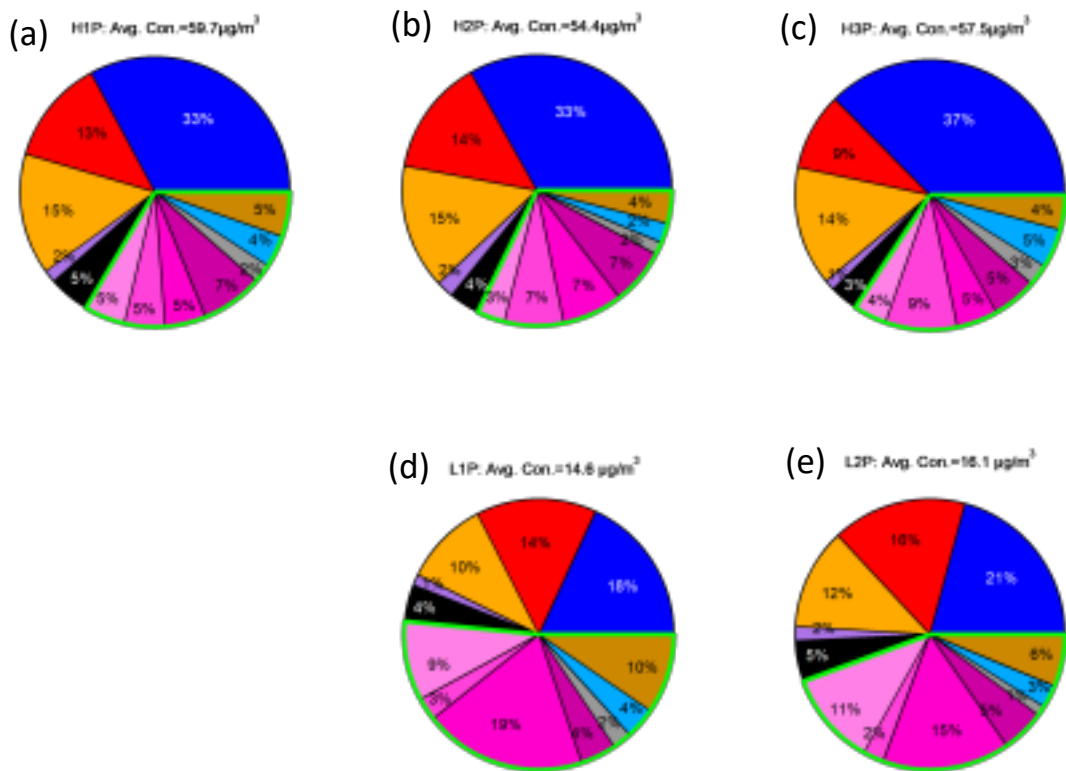
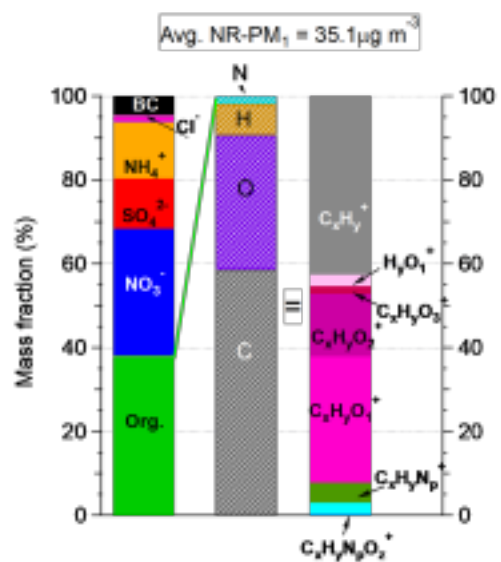


**Figure S11.** Averaged compositional pie chart of PM<sub>1</sub> species (non-refractory-PM<sub>1</sub> plus black carbon (BC)) in **(a-c)** three haze episodes and **(d, e)** two clean periods.

272



273

274

275

276

277

278 **Figure S12.** Overview of the OA compositions in SMA during entire study (early spring of 2019)

279

280

281

282

283

284

285

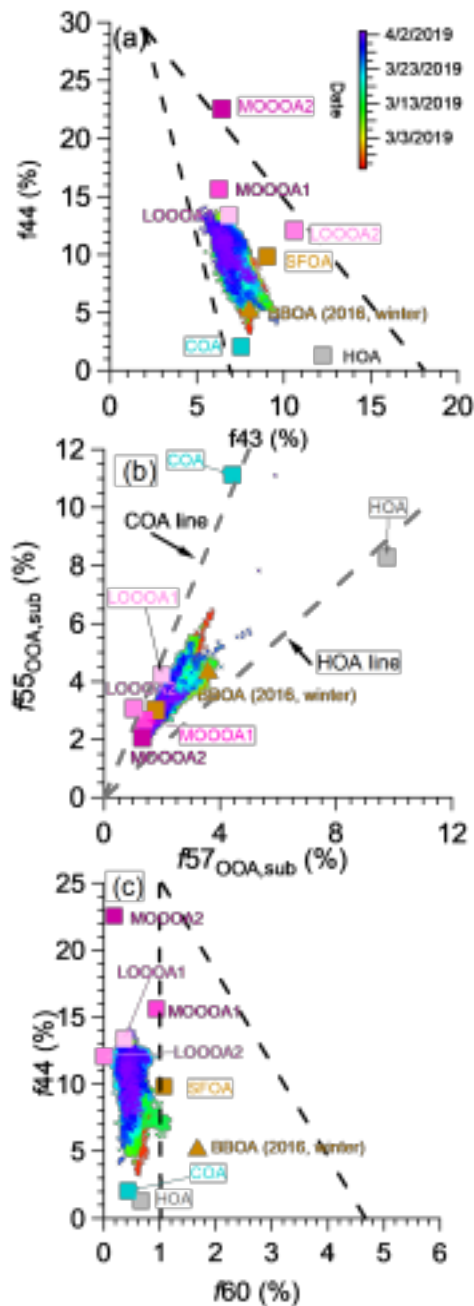
286

287

288

289

290  
 291  
 292  
 293  
 294  
 295  
 296  
 297  
 298  
 299  
 300  
 301  
 302  
 303  
 304  
 305  
 306  
 307  
 308  
 309



310 **Figure S13.** Triangular plots of (a)  $f_{44}$  versus  $f_{43}$  (b)  $f_{55, \text{OOA, sub}}$  versus  $f_{57, \text{OOA, sub}}$  and (c)  $f_{44}$  versus  
 311  $f_{60}$  for the seven OA factors and all of the measured OA data (dots), colored by the time of the  
 312 day.  $f_{43}$ ,  $f_{44}$ , and  $f_{60}$  are the ratios of the organic signal at  $m/z = 43, 44,$  and  $60$  to the total organic  
 313 signal in the component mass spectrum, respectively.  $f_{55, \text{OOA, sub}}$  and  $f_{57, \text{OOA, sub}}$  are the ratios of  
 314 the organic signal at  $m/z 55, 57$  after subtracting the contributions from LO-OOA1, LO-OOA2,  
 315 MO-OOA1 and MO-OOA2 (e.g.,  $f_{55, \text{OOA, sub}} = m/z 55 - m/z 55_{\text{LO-OOA1}} - m/z 55_{\text{LO-OOA2}} - m/z 55_{\text{MO-OOA1}} -$   
 316  $m/z 55_{\text{MO-OOA2}}$ ;  $f_{57, \text{OOA, sub}} = m/z 57 - m/z 57_{\text{LO-OOA1}} - m/z 57_{\text{LO-OOA2}} - m/z 57_{\text{MO-OOA1}} - m/z 57_{\text{MO-OOA2}}$ ).  
 317 2016 winter BBOA is also shown with triangle for the comparison (Kim et al., 2017)

318  
319  
320  
321  
322  
323  
324  
325  
326  
327  
328  
329  
330  
331  
332  
333  
334  
335  
336  
337  
338  
339  
340  
341  
342

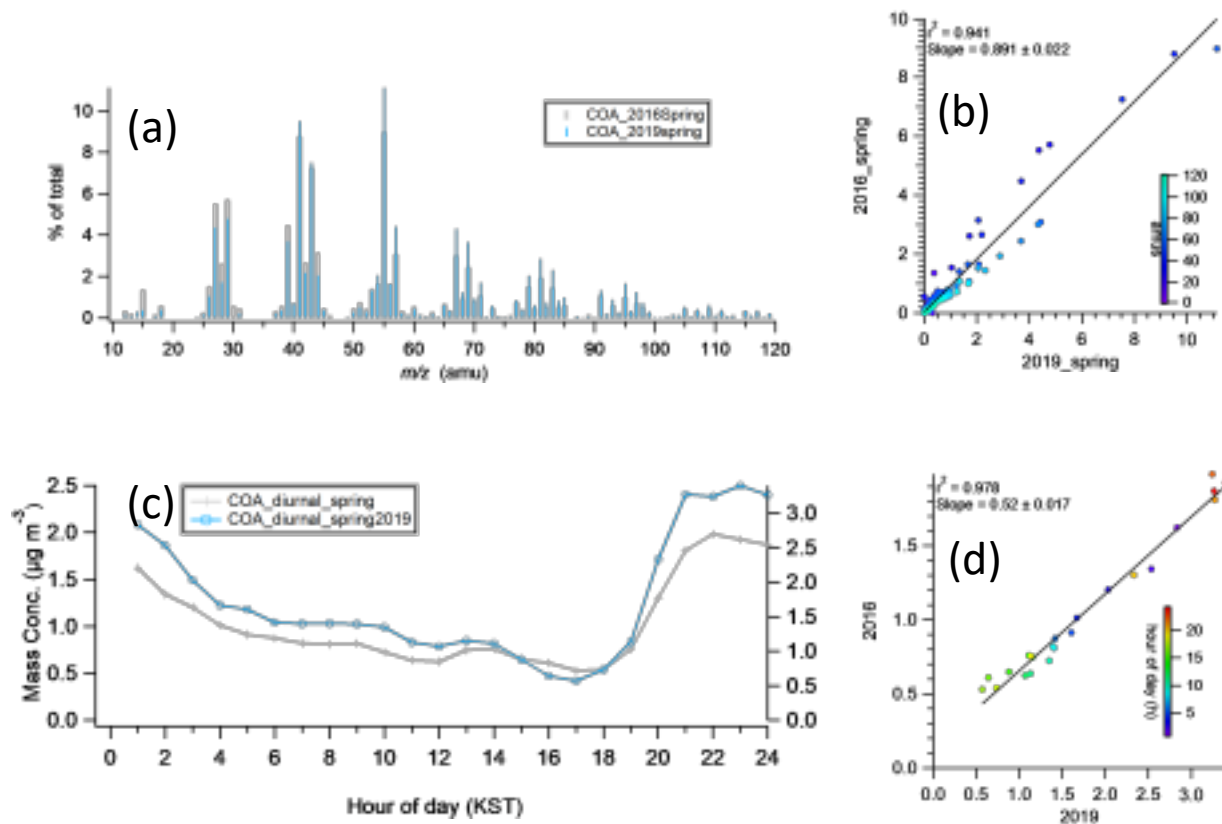


**Figure S14.** (a) mass spectra of the COAs from this study (spring) and the one from KORUS-AQ (Kim et al., 2018); (b) scatter plots of both COA mass spectra; (c) diurnal profile of the COAs from this study (spring) and the one from KORUS-AQ (Kim et al., 2018); and (d) scatter plots of both COA diurnal profile.

343  
 344  
 345  
 346  
 347  
 348  
 349  
 350  
 351  
 352  
 353  
 354  
 355  
 356

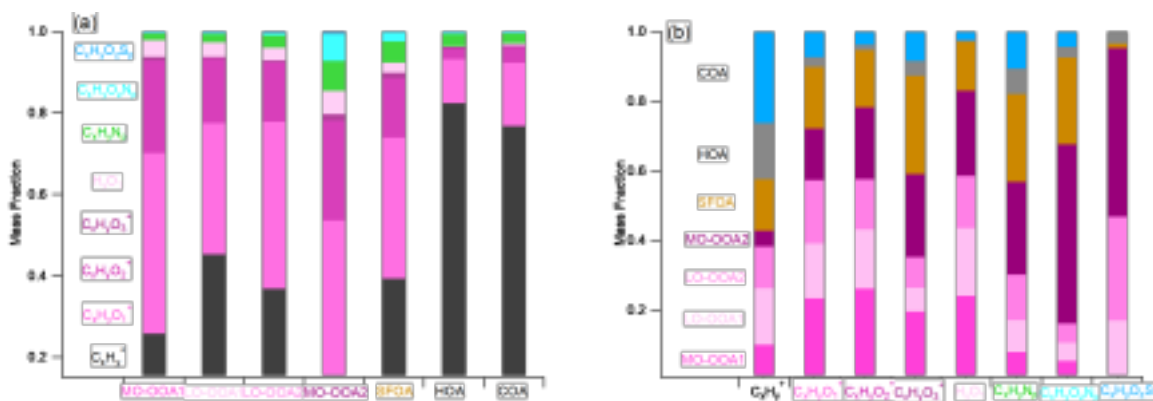
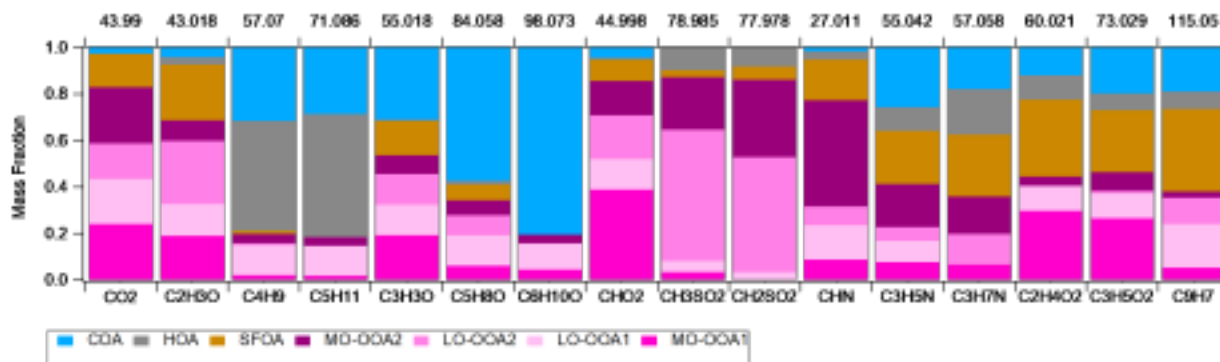
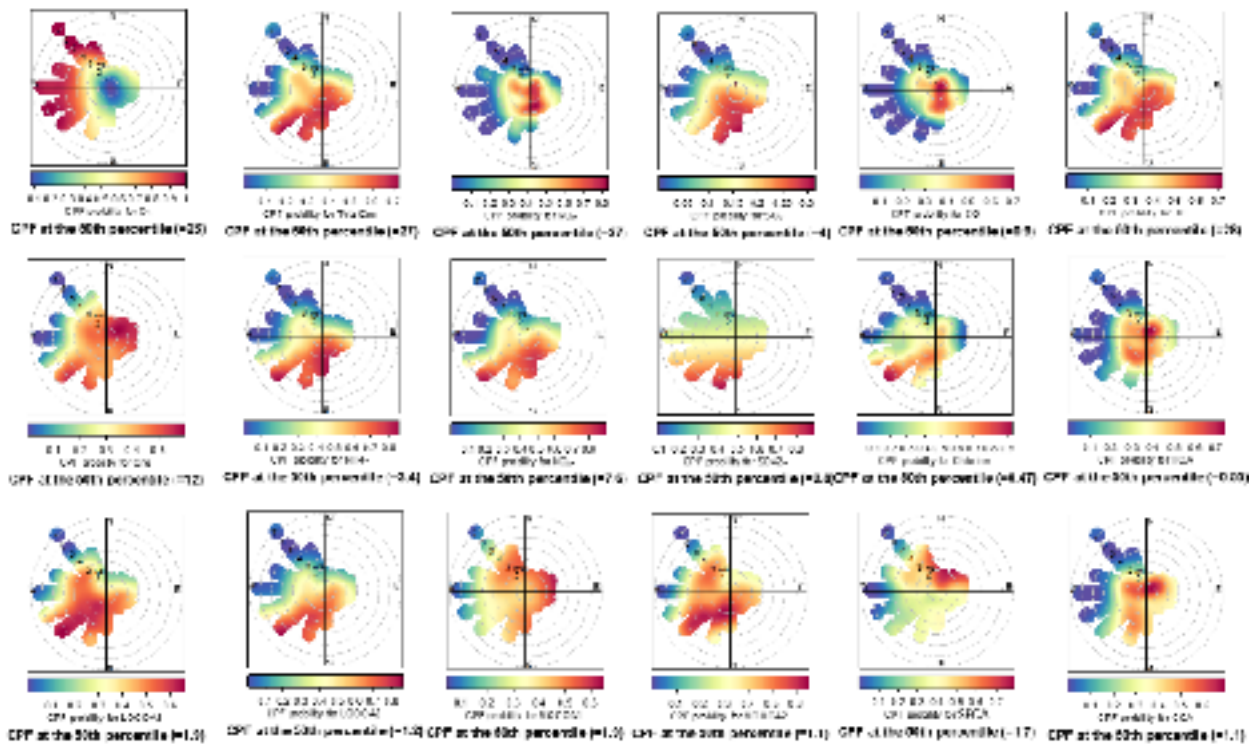


**Figure S15.** (a) Average mass fractional contributions of seven ion families to each of the OA factors and; (b) Average mass fractional contributions of seven OA factors to 8 each ion families



357  
 358  
 359  
 360  
 361

**Figure S16.** Mass fractional contribution of the seven factors from PMF analysis to various ions that are relevant to each significant tracer.



362

363

364

365

366 **Figure S17.** Conditional probability function of hourly averaged total PM<sub>1</sub> +BC, BC and mixing  
 367 ratios various gas phase species concentrations (top row), hourly averaged total PM<sub>1</sub> species  
 368 (middle row), and mass concentrations of the seven OA factors identified from PMF analysis  
 369 (bottom row) as a function of WS and direction.

370

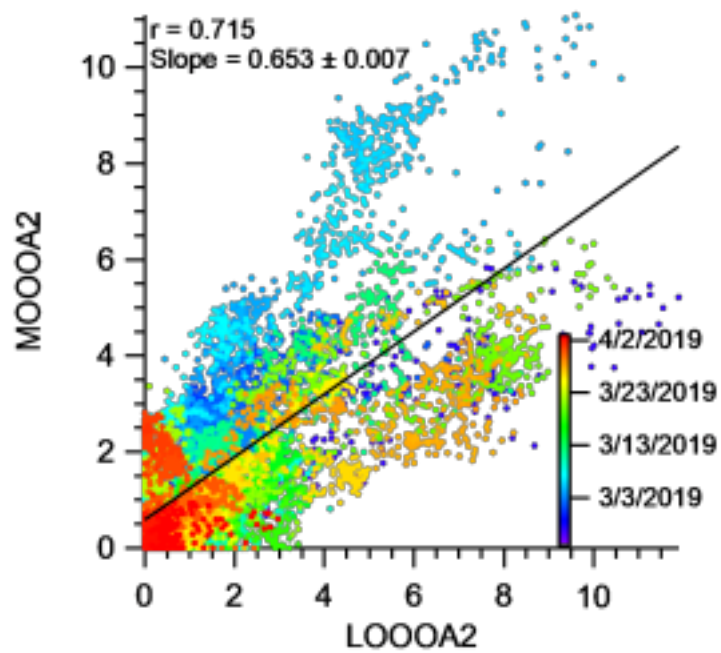
371

372

373

374

375



376

377

378

379 **Figure S18.** Correlations between MO-OOA2 and LO-OOA2 colored with date and time.

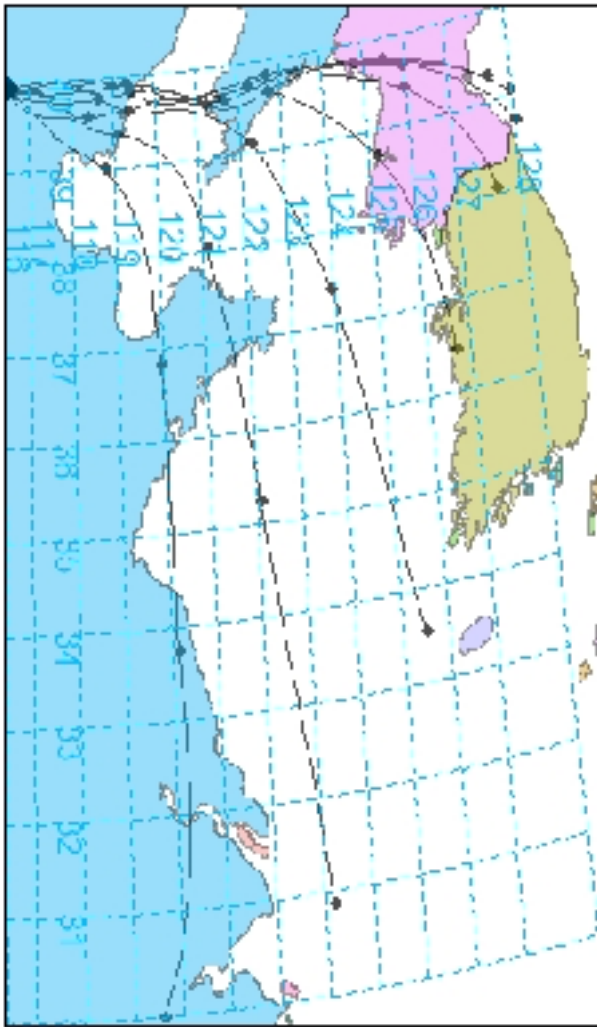
380

381

382

383

384



385

386 **Figure S19.** Forward trajectory from Beijing measurement site

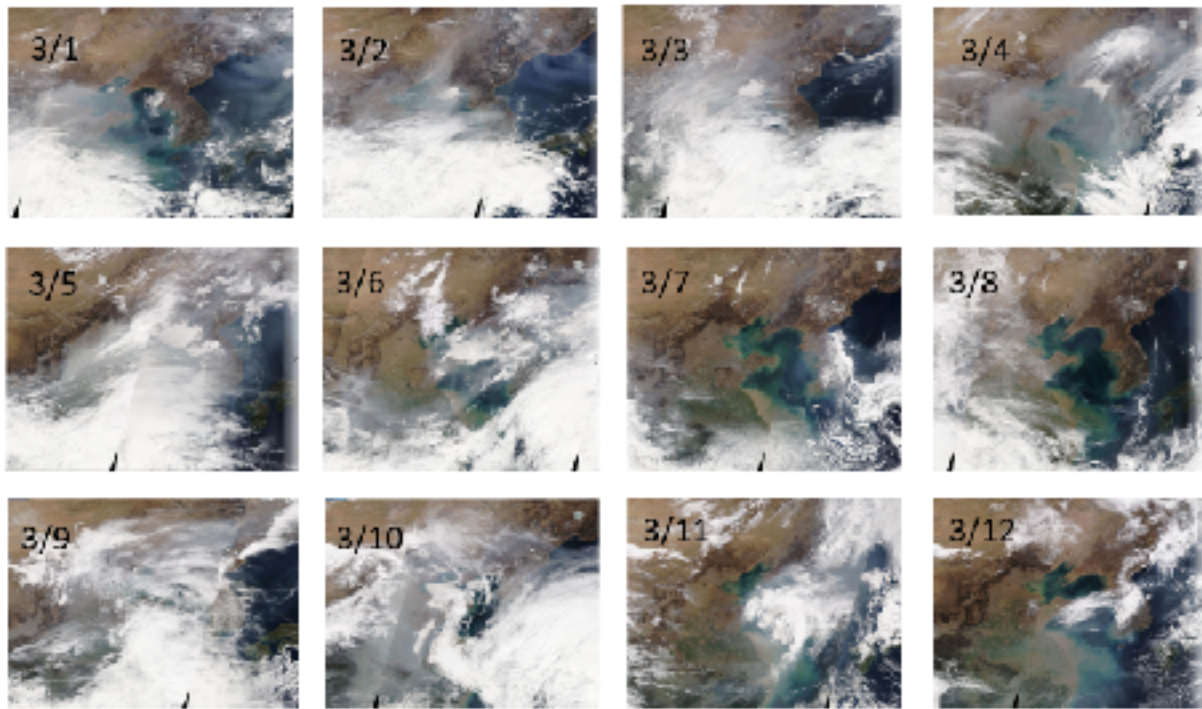
387

388

389

390





391

392

393

394

395 **Figure S20.** Long range transportation of plums from China to Korea during Haze period. Plots  
 396 are from MODIS, terra.

397

398

399

400

401

402

403

404

405  
 406  
 407  
 408  
 409  
 410  
 411  
 412  
 413  
 414  
 415  
 416  
 417  
 418  
 419  
 420  
 421  
 422  
 423  
 424  
 425  
 426  
 427  
 428  
 429  
 430  
 431

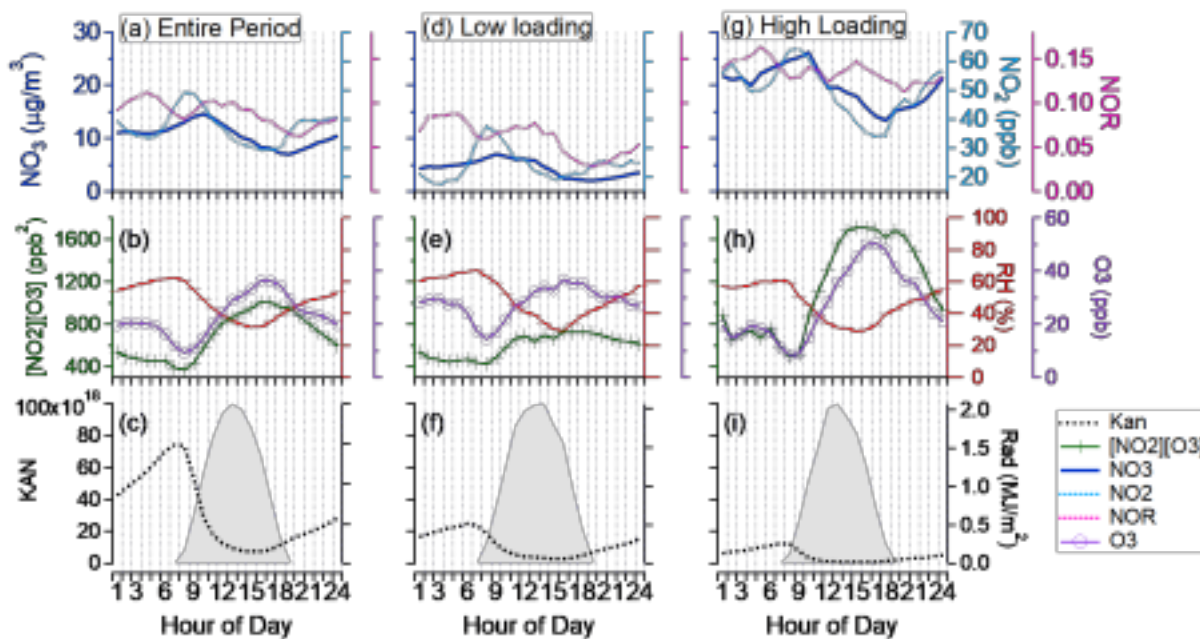


**Figure 21.** One-hour averaged diurnal profiles for nitrate and various parameters and proxies for formation pathways in entire, haze and clean period during 2019 spring; Temperature, relative humidity and KAN as the equilibrium constant for gas-to-particle partitioning for ammonium nitrate in (a-c) entire period (d-f) low loading period and (g-i) high loading period. Note that the one-hour averaged diurnal profiles of NO<sub>2</sub>, NO<sub>3</sub>, [NO<sub>2</sub>][O<sub>3</sub>] as a proxy for nighttime formation of HNO<sub>3</sub> and subsequently particulate nitrate, and [NO<sub>2</sub>] times solar radiation as a proxy for daytime HNO<sub>3</sub> formation are shown

432  
433  
434  
435  
436  
437  
438  
439  
440  
441  
442  
443  
444  
445  
446  
447  
448  
449  
450  
451  
452  
453  
454

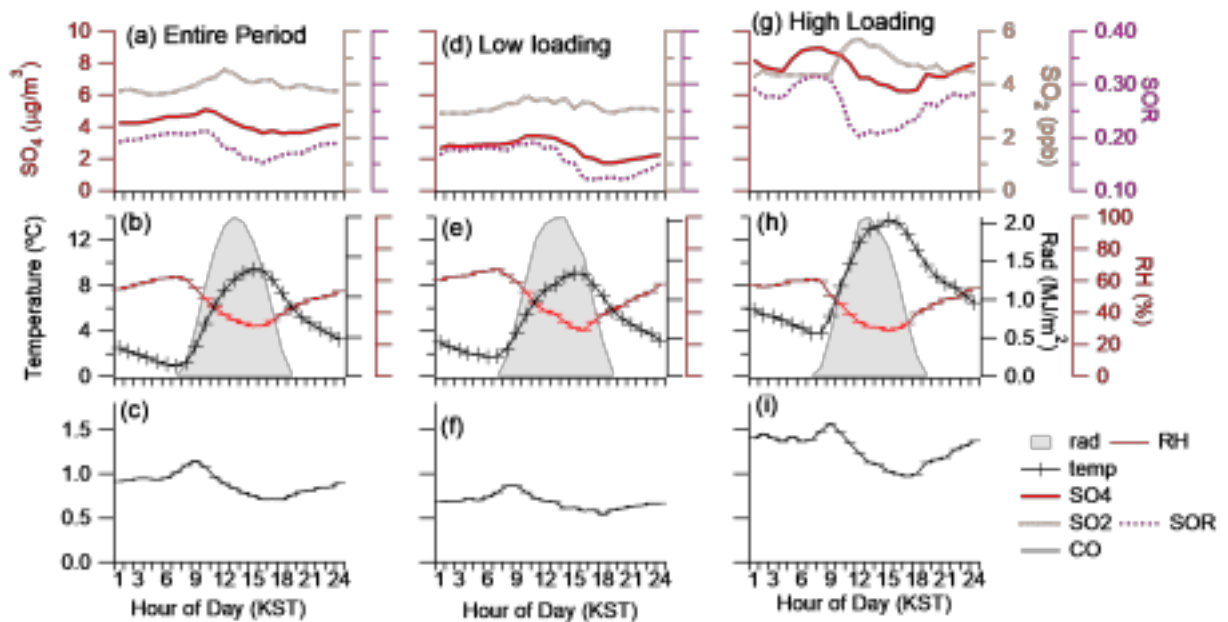


**Figure S22.** One-hour averaged diurnal profiles for nitrate and various parameters and proxies for formation pathways in entire, haze and clean period during 2019 spring; Temperature, relative humidity and solar radiation as a proxy for daytime H<sub>2</sub>SO<sub>4</sub> formation in (a-c) entire period (d-f) low loading period and (g-i) high loading period.

455  
456  
457  
458  
459  
460  
461  
462  
463  
464  
465  
466  
467  
468  
469  
470  
471  
472  
473  
474  
475  
476  
477

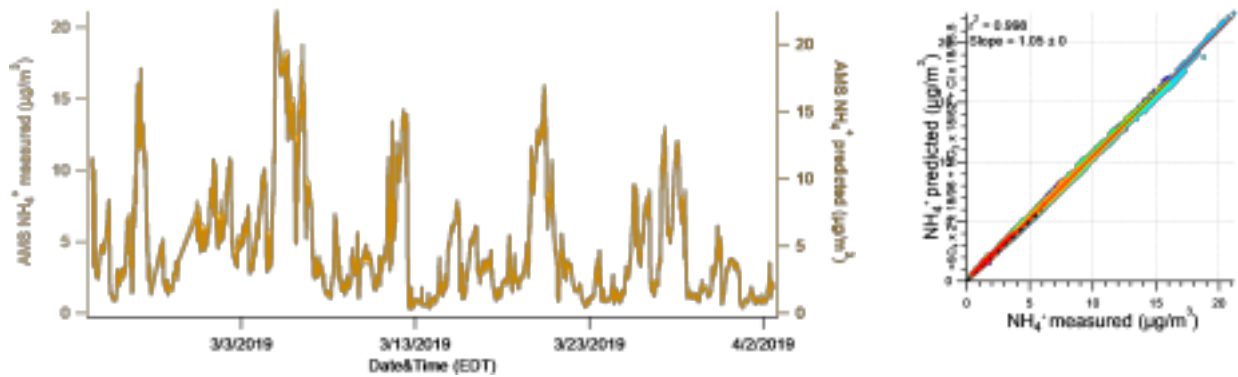


**Figure S23.** Time series (a) and Scatterplot (b) that compares predicted  $\text{NH}_4^+$  versus measured  $\text{NH}_4^+$  concentrations. The predicted values were calculated assuming full neutralization of the anions (e.g., sulfate, nitrate, and chloride). The data points are colored by date.

478 **References**

- 479
- 480 Aiken, A. C., Decarlo, P. F., Kroll, J. H., Worsnop, D. R., Huffman, J. A., Docherty, K. S., Ulbrich, I. M.,  
481 Mohr, C., Kimmel, J. R., Sueper, D., Sun, Y., Zhang, Q., Trimborn, A., Northway, M., Ziemann, P. J.,  
482 Canagaratna, M. R., Onasch, T. B., Alfarra, M. R., Prevot, A. S. H., Dommen, J., Duplissy, J., Metzger,  
483 A., Baltensperger, U., and Jimenez, J. L.: O/C and OM/OC ratios of primary, secondary, and ambient  
484 organic aerosols with high-resolution time-of-flight aerosol mass spectrometry, *Environmental Science*  
485 *& Technology*, 42, 4478-4485, 10.1021/es703009q, 2008.
- 486 Canagaratna, M. R., Jimenez, J. L., Kroll, J. H., Chen, Q., Kessler, S. H., Massoli, P., Hildebrandt Ruiz, L.,  
487 Fortner, E., Williams, L. R., Wilson, K. R., Surratt, J. D., Donahue, N. M., Jayne, J. T., and Worsnop,  
488 D. R.: Elemental ratio measurements of organic compounds using aerosol mass spectrometry:  
489 characterization, improved calibration, and implications, *Atmospheric Chemistry and Physics*, 15, 253-  
490 272, 10.5194/acp-15-253-2015, 2015.
- 491 Kim, H., Zhang, Q., Bae, G. N., Kim, J. Y., and Lee, S. B.: Sources and atmospheric processing of winter  
492 aerosols in Seoul, Korea: insights from real-time measurements using a high-resolution aerosol mass  
493 spectrometer, *Atmos. Chem. Phys.*, 17, 2009-2033, 10.5194/acp-17-2009-2017, 2017.
- 494 Kuwata, M., Zorn, S. R., and Martin, S. T.: Using Elemental Ratios to Predict the Density of Organic  
495 Material Composed of Carbon, Hydrogen, and Oxygen, *Environmental Science & Technology*, 46,  
496 787-794, 10.1021/es202525q, 2012.
- 497 Middlebrook, A. M., Bahreini, R., Jimenez, J. L., and Canagaratna, M. R.: Evaluation of Composition-  
498 Dependent Collection Efficiencies for the Aerodyne Aerosol Mass Spectrometer using Field Data,  
499 *Aerosol Science and Technology*, 46, 258-271, 10.1080/02786826.2011.620041, 2012.
- 500 Zhang, Q., Canagaratna, M. R., Jayne, J. T., Worsnop, D. R., and Jimenez, J. L.: Time- and size-resolved  
501 chemical composition of submicron particles in Pittsburgh: Implications for aerosol sources and  
502 processes, *Journal of Geophysical Research-Atmospheres*, 110, 10.1029/2004jd004649, 2005.

503

504